Contents lists available at ScienceDirect

Mechatronics

journal homepage: www.elsevier.com/locate/mechatronics

Control and experiments of a novel tiltable-rotor aerial platform comprising quadcopters and passive hinges☆,☆☆

Lecheng Ruan [a,*,1], Chen-Huan Pi [b,1], Yao Su [a,*], Pengkang Yu [a], Stone Cheng [b], Tsu-Chin Tsao [a]

[a] Mechanical and Aerospace Engineering Department, University of California, Los Angeles, Los Angeles, United States of America
[b] Mechanical Engineering Department, National Yang Ming Chiao Tung University, HsinChu, Taiwan

ARTICLE INFO

Keywords:
Multirotor
Overactuation
Six DoF control
Optimal control allocation
Flight experiment

ABSTRACT

This paper presents the control and experiment of a novel multirotor aerial platform, which is capable of full actuation for six Degree of Freedom (DoF) motions. The platform is actuated by a number of tilting-thrust modules, each consisting of a regular quadcopter and a mechanically passive hinge. The platform in this paper has four such actuator modules, making an over-actuated system that requires input allocations in the feedback control. In addition to the common least-square method that minimizes the sum of squares of the thrusts, we propose a control allocation that minimizes the maximum thrust in a closed-form analytical solution for efficient real time computation. This allocation can achieve larger inclination angles than that by the least-square method, when thrust forces are insufficient to overcome the gravity for all poses. Simulation and real world experiments are presented to demonstrate the control of the aerial platform for six DoF motion tracking and disturbance rejection.

1. Introduction

Multirotors, among various unmanned aerial vehicles (UAVs) that have caught interests in research and applications recently, have advantages in mechanical simplicity, high agility, vertical take-off and landing(VTOL), and hovering capability. Traditional multirotor platforms usually align multiple propellers in the same direction to effectively compensate for the gravity during the flight. This configuration is underactuated, but is proven differential-flat [1] for the independent control of a four DoF subspace [2,3], which is adequate for position-oriented applications such as surveillance, rescue, delivery, inspection and mobile network construction, etc. [4–12].

The regular multirotors cannot control position and attitude independently due to the intrinsic underactuation. This limits their applications where six DoF control is required, such as the exploration in complicated terrains [13] or multi-pose interaction with the environment [14]. These requirements have motivated the designs of fully actuated multirotor platforms, which are categorized into two major classes [15]. The first class [16–19] deploys at least six propellers at various fixed orientations for six DoF actuation, and inherits the mechanical simplicity of regular multirotors. However, the thrust capability in different DoFs has large disparities and cannot be changed once the propeller directions are fixed. Therefore, the configurations must be designed to meet the requirements of specific applications [16,17].

The second class actively controls the attitude of each propeller [20–24], referred to as the tiltable-rotor aerial platforms in the rest of this paper. This concept was first proposed and realized by [20], where the propeller angles of a quadcopter platform are actively controlled by servo motors. The enhanced flexibility and configurability of these platforms are accompanied by significantly increased mechanical complexity and weights. Therefore, only a limited number of designs have been realized and experimentally validated [20,21,24]. The tiltable-rotor platforms introduce three issues that are not existent in regular quadcopters. The first issue is that the aerodynamic drag torques of the propellers, when at different cant angles, cannot cancel one another like those of the quadcopters. The second issue is that the tilting-thrust actuators exert reaction torques to the central frame when tilting. The third issue is that the gyroscopic torques occur for each propeller–rotor when changing directions. In the control system design, these three issues have been commonly treated as disturbances or unmodeled dynamics.

Most fully actuated multirotor platforms have input redundancies and require allocation schemes to map the desired torque and force

☆ This paper was recommended for publication by Associate Editor Weichao Sun.
☆☆ The supplementary video of real-world experiments is available at https://www.youtube.com/watch?v=ERbJaznHi-c.
* Corresponding author.
E-mail addresses: ruanlecheng@ucla.edu (L. Ruan), yaosu@ucla.edu (Y. Su).
[1] The first two authors contributed equally to this work. CP. Pi and S. Cheng were visiting UCLA during this work.

https://doi.org/10.1016/j.mechatronics.2022.102927
Received 25 January 2022; Received in revised form 3 November 2022; Accepted 21 November 2022

to the physical inputs, usually the thrust force and orientation of each propeller. To this end, the least-square approach is commonly used for its simplicity and robustness [21,22]. This approach is based on a linear force decomposition, where the least-square method is applied to some intermediate variables, followed by a nonlinear mapping from the optimal solution to the physical input variables. As such, the optimal solution for the intermediate variables may not carry a physical meaning. In view of this, [20] formulate the allocation optimization based on the physical input variables to account for physical constraints, but the gradient-based numerical iterations in every control update require significant real-time computation.

Regular quadcopters can provide variable total thrust force while simultaneously regulating their attitude [1], thus can be used to replace the rotor and tilting motor pair. Cables [25,26] or universal joints [27] have been used to connect multiple quadcopters to the tool frame for cooperative manipulations. However, the limited range of the tensioned cables or spherical joints used to connect quadcopters and the tool frame significantly constrains the achievable attitudes. Our group has proposed modular vectored thrust units made of quadcopters and passive mechanisms without angle range limits or constraints for two realizations, one DoF hinge [28,29] or two DoF gimbal [30,31]. These modular vectored thrust units overcome the constraints of the limited orientations between the quadcopters and the main frame in [25–27], and enable creating new multirotor aerial platforms for unique capabilities and performance. Although having advantageous thrust efficiency at large attitude angles, the two DoF gimbal [30] exhibit higher complexity, weight and structural compliance than the one DoF hinge, and will encounter kinematic singularity when its two axes are co-linear.

In this paper, we present a novel low-complexity and simple-to-build fully actuated tiltable-rotor aerial platform [28,29]. Our presented platform has unlimited joint angle ranges and greatly reduces the mechanical complexity, compared to existing tiltable-rotor configurations where the tilting of each rotor is actuated by a servo motor. An important feature of our tiltable-rotor platform is the elimination of the propeller drags, gyroscopic momentums and tilting reaction torques, which had been treated as disturbances or unmodeled dynamics in other tiltable-rotor platforms, because of the paired propellers rotating in opposite directions and the zero-torque transmission in the passive hinges. We have presented the preliminary work on the control experiment using a heuristic allocation method in [29]. In this paper, we will present closed-form optimal solutions for min–max input allocations for higher thrust efficiency, and comprehensive simulation and experiments to demonstrate the platform and controller's capabilities. Our contributions, significantly extended from [29], are highlighted in the followings:

(1) We will analyze the dynamics of our aerial platform and provide a comprehensive comparison with other related configurations to show the advantages of eliminating the aerodynamic drag forces, gyroscopic momentums and tilting reaction torques that are regarded as disturbances in tiltable rotor configurations driven by propeller–rotor pairs, and furthermore, the unique high-bandwidth auxiliary torque inputs to perform control compensations and actuator failure recovery, which are unavailable to other tiltable rotor realizations or the two DoF gimbal configuration.
(2) We will formulate and analytically solve the min–max optimal allocation to suppress the maximum required thrust and thus achieve a larger operational space under input saturation compared with existing allocations. This method will also facilitate real-time implementation without numerical iterations for solving optimization. We will also provide a quantitative stability criterion for the presented hierarchical control architecture.
(3) We will provide simulation and experimental validations to demonstrate the platform's capability of full actuation, the effectiveness of the min–max optimal allocation to achieve a larger operational space subject to the maximum thrust limits, and the stability and disturbance rejection capability of the presented control architecture.

The rest of this paper is organized in the following structure. Section 2 illustrates the mechanical design and dynamics of the presented platform, and conduct a comprehensive comparison with existing tiltable-rotor multirotor aerial platforms. Section 3 presents the hierarchical control architecture and the stability analysis of the platform, while elaborating the formulation of the min–max optimal allocation and its analytical solution. Section 4 demonstrates the simulation and experiment verifications. The paper is discussed and concluded in Section 5 and Section 6 respectively.

2. Platform

2.1. Structure and dynamics

The mechanical structure of the presented platform is demonstrated in Fig. 1. The central frame is composed of four carbon fiber tubes perpendicularly installed on the central connector. A regular quadcopter is passively hinged to each carbon fiber tube by a connector with an embedded nylon bearing. The relative motion of the quadcopter with respect to the central frame is restrained merely to the rotation along the tube, denoted as α_i for quadcopter i. l refers to the platform arm length, a the quadcopter arm length, and r the propeller radius of each quadcopter. It has been analyzed in [29] that each quadcopter in the presented platform has more than the full functionalities of a propeller with active tiltable cant angle, as in the previous works [20–22].

The platform dynamics is equivalent to a rigid body with exerted forces and torques of varying magnitudes and directions [29]. As shown in Fig. 1, the world inertial frame, body frame and quadcopter frames are defined as

$$\begin{aligned} &\mathcal{F}_W : \{O; \boldsymbol{x}, \boldsymbol{y}, \boldsymbol{z}\}, \\ &\mathcal{F}_B : \{O_B; \boldsymbol{x}_B, \boldsymbol{y}_B, \boldsymbol{z}_B\}, \\ &\mathcal{F}_{Q_i} : \{O_{Q_i}; \boldsymbol{x}_{Q_i}, \boldsymbol{y}_{Q_i}, \boldsymbol{z}_{Q_i}\}, \end{aligned} \tag{1}$$

respectively, where $i = 0, 1, 2, 3$ and $j = 0, 1, 2, 3$ refers to the orders of the quadcopters and propellers.

Primary Inputs: It has been stated in [29] that the four propeller–rotor pairs in quadcopter i collectively generate four independent inputs in its quadcopter frame $\mathcal{F}_{Q_i}$ as

$$\boldsymbol{U}_i = \begin{bmatrix} T_i & M_i^x & M_i^y & M_i^z \end{bmatrix}^T = \boldsymbol{T}_Q \boldsymbol{\Omega}_i, \tag{2}$$

where T_i refers to the collective total thrust force, M_i^x, M_i^y, M_i^z the collective total torques along the x_{Q_i}, y_{Q_i} and z_{Q_i} directions. $\boldsymbol{\Omega}_i$ is the propeller speed vector where each element can be controlled independently, and $\boldsymbol{T}_Q$ is a constant matrix dependent merely on the quadcopter and propeller properties. The propeller speed is usually, if not always, considered to be of zero-order dynamics as the inertia of the propeller–rotor pairs is neglectable compared with the quadcopter or frame inertia. Therefore, the four inputs in $\boldsymbol{U}$ are regarded as the primary inputs of the platform dynamics.

Translational Dynamics: The translational motion of the platform is actuated by the four total thrust forces T_i on each quadcopter. Denoting m and $\boldsymbol{G}$ as the platform mass and the gravitational acceleration, and defining the platform center-of-mass position as $\boldsymbol{\xi} = \begin{bmatrix} x & y & z \end{bmatrix}^T$, the translational motion can be calculated by Newton's Second Law as

$$\ddot{\boldsymbol{\xi}} = \frac{1}{m} {}^W\boldsymbol{R}_B \left(\sum_{i=0}^{3} {}^B\boldsymbol{R}_{Q_i} \boldsymbol{T}_i\right) + \boldsymbol{G}, \tag{3}$$

where each total thrust force T_i on quadcopter i is transformed to the platform body frame $\mathcal{F}_B$ by ${}^B\boldsymbol{R}_{Q_i}$, summed up and transformed collectively to the world frame $\mathcal{F}_W$ by ${}^W\boldsymbol{R}_B$. Notice that the transformation matrix ${}^B\boldsymbol{R}_{Q_i}$ from each quadcopter to the platform body frame is a

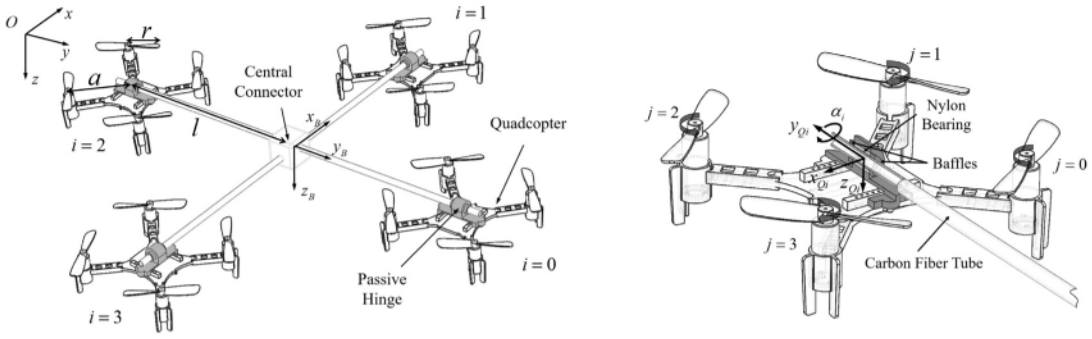

(a) The presented tiltable-rotor aerial platform.

(b) The tilting-thrust actuator comprising of regular quadcopter and passive hinge.

Fig. 1. Configuration of the presented tiltable-rotor aerial platform. Regular quadcopters are mounted on mechanically passive hinges as tilting-thrust actuators. The world frame $\mathcal{F}_W$ is defined under the North-East-Down (NED) convention. The body frame $\mathcal{F}_B$ origin is located at the geometric center of the central connector. x_B and y_B are aligned with the carbon fiber tubes. The quadcopter frames $\mathcal{F}_{Q_i}$ is attached with each quadcopter. y_{Q_i} is aligned with the hinge axis, and z_{Q_i} crosses the quadcopter geometric center.

function of the corresponding tilting angle α_i, and matrix ${}^W\boldsymbol{R}_B$ is a function of the platform attitude, usually denoted by a set of Euler angles $\boldsymbol{\eta} = \begin{bmatrix}\phi & \theta & \psi\end{bmatrix}^T$, as stated in [29].

Rotational Dynamics: Denote the total external torque exerted on the platform as $\boldsymbol{\tau}$ in the platform body frame $\mathcal{F}_B$, and define the angular velocity vector in the platform body frame $\mathcal{F}_B$ as $\boldsymbol{\nu} = \begin{bmatrix}p & q & r\end{bmatrix}^T$, the rotational dynamics can be simply written as

$$\dot{\boldsymbol{\nu}} = \boldsymbol{I}^{-1}(-\boldsymbol{\nu} \times (\boldsymbol{I}\boldsymbol{\nu}) + \boldsymbol{\tau}). \tag{4}$$

The total controlled external torque is dependent on the primary inputs in $\boldsymbol{U}_i$ and mainly consists of two parts. The first part is generated collectively by the total thrust forces T_i of the four quadcopters as

$$\boldsymbol{\tau}_T = \begin{bmatrix} -c\alpha_0 l & 0 & c\alpha_2 l & 0 \\ 0 & c\alpha_1 l & 0 & -c\alpha_3 l \\ s\alpha_0 l & s\alpha_1 l & s\alpha_2 l & s\alpha_3 l \end{bmatrix} \begin{bmatrix} T_0 \\ T_1 \\ T_2 \\ T_3 \end{bmatrix}, \tag{5}$$

where $\sin\cdot$ and $\cos\cdot$ are denoted as $s\cdot$ and $c\cdot$ for simplicity. The second part is related to the total torques of each quadcopter in the primary input set, M_i^x, M_i^y and M_i^z. It can be observed in Fig. 1(b) that M_i^y is along the direction of the passive hinge and cannot be exerted on the platform. The relative motions along the directions of M_i^x and M_i^z with respect to the platform are constrained, so these torques can be directly transferred to the central frame, whose total effect can be calculated as

$$\boldsymbol{\tau}_M = \sum_{i=0}^{3} {}^B\boldsymbol{R}_{Q_i} \begin{bmatrix} M_i^x \\ 0 \\ M_i^z \end{bmatrix}. \tag{6}$$

Therefore, the total external torque exerted on the presented platform can be represented by the total controlled external torque

$$\boldsymbol{\tau} = \boldsymbol{\tau}_T + \boldsymbol{\tau}_M. \tag{7}$$

Tilting Dynamics: It can be observed that transition matrices ${}^B\boldsymbol{R}_{Q_i}$ are involved in both translational and rotational dynamics bu changing the directions of the primary inputs $\boldsymbol{U}_i$. ${}^B\boldsymbol{R}_{Q_i}$ are merely dependent on the tilting angles of quadcopters α_i, which are controlled by the primary inputs M_i^y as

$$\ddot{\alpha}_i = M_i^y - s(\frac{\pi}{2}i)\dot{p} - c(\frac{\pi}{2}i)\dot{q}. \tag{8}$$

2.2. Comparisons of tiltable-rotor platforms

To date, there are two major configurations of tiltable-rotor multirotor aerial platforms. One is realized by installing an additional actuator to actively tilt each propeller–rotor pair (denoted as **C1**) [20,21], and the other is to mount regular quadcopters onto the platform with passive hinges to unify tilting and thrusting actuations. The latter configuration has two DoF gimbal realization (denoted as **C2**), as presented in [30], and one DoF hinge realization (denoted as **C3**), as presented in this paper and [29]. This section compares these three types of platforms in various aspects, as presented in Table 1. Detailed explanations are as follows.

Mechanical Complexity: **C1** requires a special design to install the tilting actuators on the platform and house the propeller–rotor pairs on the tilting actuators. **C2** only needs to design the passive gimbal, but the complexity of the gimbal mechanism is high. **C3** only requires the design of the hinge connector with no inner mechanism, and is easily scalable for frames and quadcopters of various sizes.

Propeller Drag Disturbance: Similar to (6), each propeller–rotor pair of **C1** or each quadcopter of **C2** also generates a torque that is directly transferred to the platform, as

$$\boldsymbol{\tau}_M = \sum_{i=0}^{3} {}^B\boldsymbol{R}_{Q_i} \begin{bmatrix} 0 \\ 0 \\ M_i^z \end{bmatrix}. \tag{9}$$

The M_i^z in **C2** and **C3** is a primary input that can be controlled independently based on (2), thus may be set to zero at all times upon requirements. However, the M_i^z in **C1** is determined by the corresponding thrust force on the same propeller–rotor pair as

$$M_i^z = (\kappa_\tau/\kappa_T)T_i, \tag{10}$$

where κ_τ and κ_T are propeller related constants. This is called the propeller drag torque, which can cancel each other or be used to control the yaw angle for regular quadcopters (as the ${}^B\boldsymbol{R}_{Q_i}$ for regular quadcopter is the identity matrix), but is usually regarded as disturbances in the tiltable-rotor platforms [20,21] as the propeller axes are not co-linear.

Fast Auxiliary Inputs & Actuator Failure Recovery: It can be observed by comparing (6) and (9) that M_i^x can directly adjust the total external torque exerted on the platform $\boldsymbol{\tau}$ for **C3**. This is called the fast auxiliary input as it has much faster dynamics (zero's order for any given α_i, feedthrough) compared with the $\boldsymbol{\tau}_T$ in (5) (second order dynamics as α need to be controlled by (8) to generate desired $\boldsymbol{\tau}_T$). This property has been found of great significance in our following works for the tracking of highly-dynamic reference signals [32] and flight recovery under certain actuator failures [33,34]. On the other hand, **C1** does not have auxiliary inputs according to (9) and (10). **C2** only have M_i^z, but the magnitude (therefore the control effort) is much smaller than M_i^x, and is usually not sufficient to handle the tracking or failure recovery tasks in [32,33].

Table 1
Comparisons of tiltable-rotor platforms (the best performance under each index is **bolded**).

Configurations	**C1:** Propeller–rotor + Motor	**C2:** Quad + 2 DoF gimbal	**C3:** Quad + 1 DoF hinge
References	[20,21]	[30]	This paper, [29]
Mechanical complexity	High in overall structure	High in gimbal mechanism	**Low**
Propeller drag disturbance	Yes	**No**	**No**
Fast auxiliary inputs	No	Neglectable	**Yes**
Actuator failure recovery	No	No	**Yes**
Tilting reaction disturbance	Yes	**No**	**No**
Propeller gyroscopic effect	High	Low	**No**
Thrust efficiency	Medium	**High**	Medium

Tilting Reaction Disturbance: The tilting actuator of **C1** is installed on the platform. Therefore, when a tilting torque is exerted on the propeller–rotor pair from the tilting actuator, a reaction torque $\boldsymbol{\tau}_{\boldsymbol{R}}$ shall be exerted reversely on the platform as

$$\boldsymbol{\tau} = \boldsymbol{\tau}_T + \boldsymbol{\tau}_M + \boldsymbol{\tau}_R. \tag{11}$$

The reaction torque $\boldsymbol{\tau}_{\boldsymbol{R}}$ is dynamic and exists whenever any $\alpha_i \neq 0$, thus can only be regarded as disturbance. Unlike **C1**, the actuator tilting of **C2** or **C3** is controlled by M_i^y (and M_i^x for **C2**), which is generated by the interaction of the propellers and the air, thus does not have tilting reaction disturbance $\boldsymbol{\tau}_{\boldsymbol{R}}$ on the platform.

Propeller Gyroscopic Effect: The propeller gyroscopic effect comes from the torque $\boldsymbol{\tau}_G$ generated from the change of total angular momentum $\boldsymbol{L}_G$ as

$$\boldsymbol{\tau}_G = \frac{d\boldsymbol{L}_G}{dt}. \tag{12}$$

In **C1**, the total angular momentum of each actuator is

$$\boldsymbol{L}_G = I_P \boldsymbol{\omega}, \tag{13}$$

where I_P is the propeller inertia and $\boldsymbol{\omega}$ the angular velocity. In **C2** and **C3**, the total angular momentum of each actuator (quadcopter) collects each propeller's angular momentum as

$$\boldsymbol{L}_G = I_p \sum_{j=0}^{3} \boldsymbol{\omega}_j. \tag{14}$$

In **C3**, for the primary inputs T_i and M_i^y, the angular velocities of $\boldsymbol{\omega}_0$ and $\boldsymbol{\omega}_1$ are always of identical magnitude and opposite direction, e.g. $\boldsymbol{\omega}_0 + \boldsymbol{\omega}_1 \equiv 0$. $\boldsymbol{\omega}_2$ and $\boldsymbol{\omega}_3$ have the same relation. Therefore, $\boldsymbol{L}_G \equiv 0$ and thus

$$\boldsymbol{\tau}_G \equiv 0 \tag{15}$$

for **C3**, e.g. the propeller gyroscopic effect is eliminated. The total angular momentum of **C2** generally does not have this property as the magnitude of each angular velocity is different when the quadcopter tilts along both axes. However, the total angular momentum of **C2** shall be much smaller than **C1** as the two oppositely rotating propeller pairs cancel a large portion of the angular momentum, so the gyroscopic effect shall be also attenuated.

Thrust Efficiency: The thrust efficiency is defined as the percentage of thrust used to compensate for platform gravity. For **C1** and **C3**, the efficiency decreases for larger platform attitudes, but is generally higher compared with regular quadcopters when allocated properly. However, it has been proved and experimentally validated in [30] that **C2** can maintain almost constant full efficiency for arbitrary attitudes.

3. Control

3.1. Dynamic model reformulation

The nonlinear platform dynamic model is reformulated in this section to accommodate linear control techniques. In this paper, only primary inputs T_i and M_i^y are used in control. M_i^x and M_i^z are assigned zero at all time. Assuming that the gyroscopic effect of the central frame is neglectable, the translational and rotational dynamics are written in the matrix form

$$\begin{bmatrix} \ddot{\boldsymbol{\xi}} \\ \dot{\boldsymbol{\nu}} \end{bmatrix} = \begin{bmatrix} \frac{1}{m}{}^W\boldsymbol{R}_B & \boldsymbol{0} \\ \boldsymbol{0} & \boldsymbol{I}_Q^{-1} \end{bmatrix} \begin{bmatrix} \boldsymbol{J}_\xi \\ \boldsymbol{J}_\nu \end{bmatrix} \boldsymbol{T} + \begin{bmatrix} \boldsymbol{G} \\ \boldsymbol{0} \end{bmatrix}, \tag{16}$$

where

$$\begin{aligned} \boldsymbol{J}_\xi &= \begin{bmatrix} -s\alpha_0 & 0 & s\alpha_2 & 0 \\ 0 & s\alpha_1 & 0 & -s\alpha_3 \\ c\alpha_0 & c\alpha_1 & c\alpha_2 & c\alpha_3 \end{bmatrix}, \\ \boldsymbol{J}_\eta &= \begin{bmatrix} -c\alpha_0 l & 0 & c\alpha_2 l & 0 \\ 0 & c\alpha_1 l & 0 & -c\alpha_3 l \\ s\alpha_0 l & s\alpha_1 l & s\alpha_2 l & s\alpha_3 l \end{bmatrix}, \\ \boldsymbol{T} &= \begin{bmatrix} T_0 & T_1 & T_2 & T_3 \end{bmatrix}^T. \end{aligned} \tag{17}$$

The rotation inertia matrix is denoted as $\boldsymbol{I}_Q$. In the dynamic model (16), T_i and α_i are controlled by the platform primary inputs T_i and M_i^y, and thus considered as inputs, but nonlinearly coupled. However, when defining the tilted thrust force vector

$$\boldsymbol{F} = \begin{bmatrix} F_{s0} & F_{c0} & \dots & F_{s3} & F_{c3} \end{bmatrix}^T, \tag{18}$$

where

$$F_{si} = s\alpha_i T_i, \quad F_{ci} = c\alpha_i T_i, \tag{19}$$

the dynamic Eq. (16) becomes linear with respect to $\boldsymbol{F}$, and can be rewritten as

$$\begin{bmatrix} \ddot{\boldsymbol{\xi}} \\ \dot{\boldsymbol{\nu}} \end{bmatrix} = \begin{bmatrix} \frac{1}{m}{}^W\boldsymbol{R}_B & \boldsymbol{0} \\ \boldsymbol{0} & \boldsymbol{I}_Q^{-1} \end{bmatrix} \boldsymbol{W}\boldsymbol{F} + \begin{bmatrix} \boldsymbol{G} \\ \boldsymbol{0} \end{bmatrix}, \tag{20}$$

where $\boldsymbol{W}$ is a full-rank constant matrix

$$\boldsymbol{W} = \begin{bmatrix} -1 & 0 & 0 & 0 & 1 & 0 & 0 & 0 \\ 0 & 0 & 1 & 0 & 0 & 0 & -1 & 0 \\ 0 & 1 & 0 & 1 & 0 & 1 & 0 & 1 \\ 0 & -l & 0 & 0 & 0 & l & 0 & 0 \\ 0 & 0 & 0 & l & 0 & 0 & 0 & -l \\ l & 0 & l & 0 & l & 0 & l & 0 \end{bmatrix}, \tag{21}$$

and can be obtained by calculating the vector $\begin{bmatrix} \boldsymbol{J}_\xi \\ \boldsymbol{J}_\nu \end{bmatrix} \boldsymbol{T}$ and rewriting each element as a linear combination of the elements in $\boldsymbol{F}$.

The new dynamic model (20) adopts tilted thrust forces $\boldsymbol{F}$ as inputs. The inputs of the original model (16)T_i and α_i can be retrieved by

$$T_i = \sqrt{F_{si}^2 + F_{ci}^2}, \tag{22}$$

$$\alpha_i = \operatorname{atan2}(F_{si}, F_{ci}), \qquad \alpha_i \in [-\pi, \pi). \tag{23}$$

The dynamic model (20) has the standard form of an over-actuated robot, thus can be further simplified by the feedback linearization technique by defining the position and attitude virtual input vectors $\boldsymbol{u}_\xi$ and $\boldsymbol{u}_\nu$, and assigning

$$\boldsymbol{F} = \boldsymbol{W}^\dagger \begin{bmatrix} m({}^W\boldsymbol{R}_B)^T & \boldsymbol{0} \\ \boldsymbol{0} & \boldsymbol{I}_Q \end{bmatrix} \left(\begin{bmatrix} \boldsymbol{u}_\xi \\ \boldsymbol{u}_\nu \end{bmatrix} - \begin{bmatrix} \boldsymbol{G} \\ \boldsymbol{0} \end{bmatrix} \right), \tag{24}$$

where $\boldsymbol{W}^\dagger$ is the Moore–Penrose pseudo inverse of $\boldsymbol{W}$ such that

$$\boldsymbol{W}\boldsymbol{W}^\dagger = \boldsymbol{I}_6. \tag{25}$$

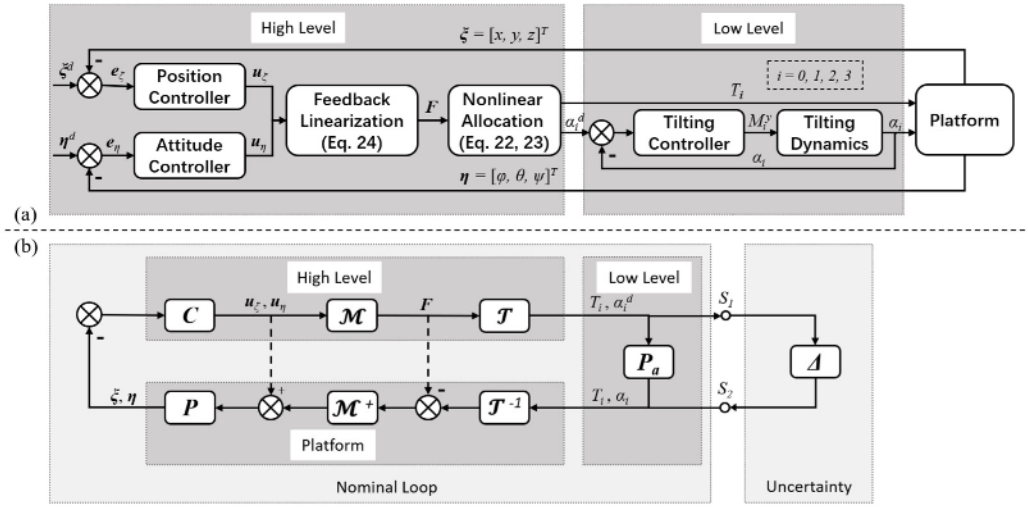

Fig. 2. (a) The presented hierarchical control architecture. The high-level position and attitude controllers generate virtual inputs for the integrator dynamics, then transformed to the desired thrust forces and tilting angles of the four quadcopters by the feedback linearization and the nonlinear allocation. The low-level controllers track the desired thrust force and tilting angle onboard each quadcopter. (b) The nominal loop is an equivalent representation of Fig. 2(a). The two dashed paths are virtual and cancel each other. The system uncertainty and approximations are represented by the uncertainty $\boldsymbol{\Delta}$.

Notice that $\boldsymbol{F}$ is in the range space of $\boldsymbol{W}^{\dagger}$ according to (24), and thus a least-square allocation [21,22].

Substituting (24) into (20) yields the final system dynamic model

$$\begin{bmatrix} \ddot{\boldsymbol{\xi}} \\ \dot{\boldsymbol{\nu}} \end{bmatrix} = \begin{bmatrix} \boldsymbol{u}_{\xi} \\ \boldsymbol{u}_{\nu} \end{bmatrix}. \tag{26}$$

3.2. Hierarchical control

As stated in the previous section, the platform dynamics has three representations, of which the progressive relationships can be clarified by the evolution of system inputs. Recall that the primary inputs of the platform are defined in (2), which are assumed to be controlled in a feedthrough manner.

Representation 1 is shown in Eq. (16), where inputs T_i are primary, and inputs α_i are controlled by primary inputs M_i^y through the second-order tilting dynamics (8). **Representation 2** is stated in (20), which uses the tilted thrust forces $\boldsymbol{F}$ in (18) as new inputs to circumvent the nonlinear coupling between T_i and α_i in Representation 1. **Representation 3** is demonstrated in (26), which absorbs the inertia, coordinate rotation and gravity into the virtual inputs $\boldsymbol{u}_{\xi}$ and $\boldsymbol{u}_{\nu}$ in (24), so that the platform dynamics is reduced to integrator dynamics.

A hierarchical control architecture is designed to cover the transitions among the three representations, as shown in Fig. 2(a). The controller is composed of high level and low level parts.

In the high level, LQRi controllers are adopted for position and attitude tracking. Define the augmented error state vectors as

$$\boldsymbol{E}_{\xi} = \begin{bmatrix} \int_0^t \boldsymbol{e}_{\xi} dt \\ \boldsymbol{e}_{\xi} \\ \dot{\boldsymbol{e}}_{\xi} \end{bmatrix}, \ \boldsymbol{E}_{\nu} = \begin{bmatrix} \int_0^t \boldsymbol{e}_{\eta} dt \\ \boldsymbol{e}_{\eta} \\ \boldsymbol{e}_{\nu} \end{bmatrix}, \tag{27}$$

where the errors are calculated by

$$\begin{aligned} \boldsymbol{e}_{\xi} &= \boldsymbol{\xi}^d - \boldsymbol{\xi}, \\ \boldsymbol{e}_{\eta} &= \tfrac{1}{2}[({}^W\boldsymbol{R}_B)^T({}^W\boldsymbol{R}_B^d) - ({}^W\boldsymbol{R}_B^d)^T({}^W\boldsymbol{R}_B)]_{\vee}, \end{aligned} \tag{28}$$

according to [35], and the operator $[\cdot]_{\vee}$ refers to the *vee* mapping from Lie algebra $\mathfrak{so}(3)$ to $\mathbb{R}^3$. The position and attitude virtual inputs are then designed by

$$\begin{aligned} \boldsymbol{u}_{\xi} &= \ddot{\boldsymbol{\xi}}^d + \boldsymbol{K}_{\xi}\boldsymbol{E}_{\xi}, \\ \boldsymbol{u}_{\nu} &= \dot{\boldsymbol{\nu}}^d + \boldsymbol{K}_{\nu}\boldsymbol{E}_{\nu}, \end{aligned} \tag{29}$$

where the state feedback gain matrices $\boldsymbol{K}_{\xi}, \boldsymbol{K}_{\nu}$ are calculated by solving the Riccati equations for error dynamics on the augmented error state vectors $\boldsymbol{E}_{\xi}$ and $\boldsymbol{E}_{\nu}$. The virtual inputs are then transformed into $\boldsymbol{F}$ by the feedback linearization (26), and further into the desired T_i and α_i by the nonlinear transformations (22) and (23).

In the low level, although T_i are primary inputs, α_i need to be controlled through the second-order tilting dynamics (8). Double-loop PID controllers are used on each quadcopter for the high-bandwidth tracking of tilting angle trajectories, as elaborated in [28].

The robust stability of the presented hierarchical control architecture has not been quantitatively addressed, even though verified on various tiltable-rotor aerial platforms through simulations and experiments [21,22,30]. This is mainly due to the high nonlinearity within the dynamics. In practice, the low-level dynamics are usually designed to be much faster than the high-level dynamics, so the overall robustness is dominated by the high-level control [36]. This section aims to develop a quantitative criterion for robust stability, under certain approximations of the system dynamics.

An alternative representation of the hierarchical control architecture is demonstrated in Fig. 2(b). It can be observed that the nominal loop is equivalent to the structure in 2(a). Here $\boldsymbol{P}$ is the integrator dynamics (26), $\boldsymbol{P}_a$ the low-level tracking dynamics for T_i and α_i, $\boldsymbol{C}$ the position and attitude controllers. $\boldsymbol{\mathcal{M}}$ and $\boldsymbol{\mathcal{M}}^{\dagger}$ refers to the forward and inverse feedback linearization, and $\boldsymbol{\mathcal{T}}$ and $\boldsymbol{\mathcal{T}}^{-1}$ the forward and inverse nonlinear transformations between $\boldsymbol{F}$ and $T_i\&\alpha_i$. The two dashed paths are virtual and cancel each other, thus do not affect the overall dynamics.

The feedback linearization block $\boldsymbol{\mathcal{M}}$ can be explicitly calculated as

$$\boldsymbol{\mathcal{M}} = \boldsymbol{W}^{\dagger}\boldsymbol{Q}, \tag{30}$$

where

$$\boldsymbol{Q} = \begin{bmatrix} \frac{1}{m}{}^W\boldsymbol{R}_B & \boldsymbol{0} \\ \boldsymbol{0} & \boldsymbol{I}_Q^{-1} \end{bmatrix}. \tag{31}$$

The nonlinear transformation $\boldsymbol{\mathcal{T}}$ can be approximated with a variational approach. When the system is disturbed by a small signal,

$$\delta \begin{bmatrix} F_{si} \\ F_{ci} \end{bmatrix} = \begin{bmatrix} s\alpha_i & c\alpha_i T_i \\ c\alpha_i & -s\alpha_i T_i \end{bmatrix} \delta \begin{bmatrix} T_i \\ \alpha_i \end{bmatrix} \triangleq \boldsymbol{\mathcal{T}}_i \delta \begin{bmatrix} T_i \\ \alpha_i \end{bmatrix}, \tag{32}$$

where δ refers to the variation operator. Therefore, the nonlinear transformation $\boldsymbol{\mathcal{T}}$ can be approximated by the linear transformation

$$\boldsymbol{\mathcal{T}} = diag(\boldsymbol{\mathcal{T}}_0, \boldsymbol{\mathcal{T}}_1, \boldsymbol{\mathcal{T}}_2, \boldsymbol{\mathcal{T}}_3). \tag{33}$$

The nominal loop gain $\boldsymbol{L}$ is then calculated by

$$\begin{aligned}\boldsymbol{L} = &\ (\mathcal{M}\boldsymbol{G}\mathcal{M}^{\dagger})(\mathcal{T}^{-1}\boldsymbol{P}_a\mathcal{T} - \boldsymbol{I}_8)\\ = &\ \boldsymbol{W}^{\dagger}\boldsymbol{Q}\boldsymbol{G}\boldsymbol{Q}^{-1}\boldsymbol{W}\mathcal{T}^{-1}(\boldsymbol{P}_a - \boldsymbol{I}_8)\mathcal{T},\end{aligned} \tag{34}$$

where $\boldsymbol{G}$ denotes the diagonal closed-loop high-level dynamics

$$\boldsymbol{G} = (\boldsymbol{I}_6 + \boldsymbol{C}\boldsymbol{P})^{-1}\boldsymbol{C}\boldsymbol{P} = \begin{bmatrix} G_p\boldsymbol{I}_3 & \boldsymbol{0} \\ \boldsymbol{0} & G_a\boldsymbol{I}_3 \end{bmatrix}. \tag{35}$$

Here each DoF of position and attitude is represented by the identical scalar transfer functions G_p and G_a respectively. Therefore, considering slow varying platform attitude, we obtain

$$\boldsymbol{Q}\boldsymbol{G}\boldsymbol{Q}^{-1} = \begin{bmatrix} G_p(\frac{1}{m}{}^{W}\boldsymbol{R}_B)\boldsymbol{I}_3(m{}^{W}\boldsymbol{R}_B^T) & \boldsymbol{0} \\ \boldsymbol{0} & G_a\boldsymbol{I}_Q^{-1}\boldsymbol{I}_Q \end{bmatrix} = \boldsymbol{G}. \tag{36}$$

The low-level dynamics $\boldsymbol{P}_a$ is diagonal, where each element is either the feedthrough thrust tracking dynamics, or the tilting angle tracking dynamics, denoted as P_a. Consider the worst-case scenario where all channels are represented by the relatively slow dynamics P_a, then

$$\mathcal{T}^{-1}(\boldsymbol{P}_a - \boldsymbol{I}_8)\mathcal{T} = (P_a - 1)\mathcal{T}^{-1}\boldsymbol{I}_8\mathcal{T} = (P_a - 1)\boldsymbol{I}_8. \tag{37}$$

The system approximations and uncertainties are represented by the uncertainty block $\boldsymbol{\Delta}$ in Fig. 2(b). Defining the uncertainty upper bound

$$\boldsymbol{\Delta} \le \Delta^U \cdot \boldsymbol{I}_8, \tag{38}$$

the robust stability criterion can be obtained by the small gain theorem

$$\begin{aligned}\|\boldsymbol{T}_C\boldsymbol{\Delta}\|_\infty &\le \|\boldsymbol{W}^{\dagger}\begin{bmatrix} \frac{G_p\Delta^U}{1+G_p(1-P_a)}\cdot\boldsymbol{I}_3 & \boldsymbol{0} \\ \boldsymbol{0} & \frac{G_a\Delta^U}{1+G_a(1-P_a)}\cdot\boldsymbol{I}_3 \end{bmatrix}\boldsymbol{W}\|_\infty \\ &< \boldsymbol{I}_8,\end{aligned} \tag{39}$$

where $\boldsymbol{T}_C$ refers to the complementary sensitivity function from S_1 to S_2 in Fig. 2(b). It can be observed that the proposed criterion reduced to the qualitative stability criterion [36] when P_a is much faster than G_p and G_a, which echos with the previous works [21,30]. Robust stability of the control architecture also indicates its capability of disturbance rejection.

3.3. Optimal allocator to suppress maximum required thrust

Using eight DoF input $\boldsymbol{F}$ to represent the six DoF virtual inputs $\boldsymbol{u}_\epsilon$ and $\boldsymbol{u}_\nu$ has multiple solutions, including the least-square allocation (24) widely used in previous works [21,30,31]. Actually, it can be observed from (20) that adding any components from the nullspace of $\boldsymbol{W}$

$$\mathcal{N}(\boldsymbol{W}) = \{\boldsymbol{x} \in \mathbb{R}^8 : \ \boldsymbol{x} = \sigma_1\boldsymbol{v}_1 + \sigma_2\boldsymbol{v}_2, \forall\sigma_1,\sigma_2 \in \mathbb{R}\}, \tag{40}$$

where

$$\begin{aligned}\boldsymbol{v}_1 &= \begin{bmatrix}-1 & 1 & -1 & 1 & \boldsymbol{0}_{1\times4}\end{bmatrix}^T, \\ \boldsymbol{v}_2 &= \begin{bmatrix}\boldsymbol{0}_{1\times4} & -1 & 1 & -1 & 1\end{bmatrix}^T\end{aligned} \tag{41}$$

to $\boldsymbol{F}$ will generate a new allocation without influencing the resulting virtual inputs $\boldsymbol{u}_\epsilon$ and $\boldsymbol{u}_\nu$.

However, these different allocations do influence the calculated thrust forces T_i, according to (22). In a practical platform, the maximum thrust force provided by each quadcopter is physically constrained, and controller failure could occur when the required thrust forces exceed this limitation. This saturation effect also limits the operational space of the platform as the thrust efficiency decreases with larger attitude angle [22]. Therefore, this section provides the design process of an optimal allocator to minimize the maximum required thrust and thus achieve a larger operational space of tilting angle platforms (including the previous platforms [20,21]) under thrust limitation, compared to the least-square allocation (24).

The optimal allocator is obtained by designing the nullspace components of $\boldsymbol{F}$ to minimize the maximum required thrust

$$(\sigma_1^{opt},\sigma_2^{opt}) = \arg\min_{(\sigma_1,\sigma_2)}(\max_i T_i), \tag{42}$$

given that each element of $\boldsymbol{F}$ under translational dynamics can be written as a function of σ_1 and σ_2 as

$$\begin{aligned}F_{s0} &= -\frac{\zeta_x}{2} - \sigma_1, \quad F_{c0} = -\frac{\zeta_z}{4} - \sigma_2, \\ F_{s1} &= \frac{\zeta_y}{2} + \sigma_1, \quad F_{c1} = -\frac{\zeta_z}{4} + \sigma_2, \\ F_{s2} &= \frac{\zeta_x}{2} - \sigma_1, \quad F_{c2} = -\frac{\zeta_z}{4} - \sigma_2, \\ F_{s3} &= -\frac{\zeta_y}{2} + \sigma_1, \quad F_{c3} = -\frac{\zeta_z}{4} + \sigma_2,\end{aligned} \tag{43}$$

where ζ_x, ζ_y and ζ_z refers to the three DoF elements of virtual input $\boldsymbol{u}_\zeta$. As the platform is symmetric in the x_B and y_B directions, we constrain the scenario within the $x_bO_Bz_B$ plane for simplicity. The total thrust forces of the four quadcopters can be explicitly calculated by (22) as

$$\begin{aligned}T_0 &= \sqrt{(\frac{\zeta_x}{2} + \sigma_1)^2 + (\frac{\zeta_z}{4} + \sigma_2)^2}, \\ T_1 = T_3 &= \sqrt{\sigma_1^2 + (\frac{\zeta_z}{4} - \sigma_2)^2}, \\ T_2 &= \sqrt{(-\frac{\zeta_x}{2} + \sigma_1)^2 + (\frac{\zeta_z}{4} + \sigma_2)^2},\end{aligned} \tag{44}$$

which are convex functions of σ_1 and σ_2. Therefore, (42) is an unconstrained convex optimization, thus having a unique global optimal solution. The rest of this section will show that this solution has a closed form and can be calculated with the geometric interpretation.

Define

$$h(\sigma_1,\sigma_2) = \max_i T_i, \tag{45}$$

then it is a piece-wise function with respect to the nullspace $\mathcal{N}(\boldsymbol{W})$ as

$$h(\sigma_1,\sigma_2) = \begin{cases} T_0, & (\sigma_1,\sigma_2) \in S_0 \\ T_1, & (\sigma_1,\sigma_2) \in S_1 \\ T_2, & (\sigma_1,\sigma_2) \in S_2 \end{cases}, \tag{46}$$

where S_0 refers to the region that $T_0 \ge T_1$ and $T_0 \ge T_2$, or

$$S_0 = \{(\sigma_1,\sigma_2) : \sigma_1 \ge 0, \sigma_2 \ge -\frac{\zeta_x}{\zeta_z}\sigma_1 - \frac{\zeta_x^2}{4\zeta_z}\}; \tag{47}$$

S_2 refers to the region that $T_2 \ge T_0$ and $T_2 \ge T_1$, or

$$S_2 = \{(\sigma_1,\sigma_2) : \sigma_1 \le 0, \sigma_2 \ge \frac{\zeta_x}{\zeta_z}\sigma_1 - \frac{\zeta_x^2}{4\zeta_z}\}; \tag{48}$$

and S_1 can be calculated by the set subtraction operation

$$S_1 = \mathbb{R}^2 - S_0 - S_2. \tag{49}$$

The min–max optimization (42) then becomes the comparison of the minimal values in these three different regions, as

$$(\sigma_1^{opt},\sigma_2^{opt}) = \arg\min_{(\sigma_1,\sigma_2)}\{h_0,h_1,h_2\}, \tag{50}$$

where

$$\begin{aligned}h_0 &= \min T_0, \quad (\sigma_1,\sigma_2) \in S_0 \\ h_1 &= \min T_1, \quad (\sigma_1,\sigma_2) \in S_1 \\ h_2 &= \min T_2, \quad (\sigma_1,\sigma_2) \in S_2\end{aligned} \tag{51}$$

Each minimal value can be geometrically interpreted as a minimal distance, as shown in Fig. 3, where the points C_0, C_1, C_2 are defined as

$$\begin{aligned}C_0 &= (-\frac{\zeta_x}{2}, -\frac{\zeta_z}{4}), \\ C_1 &= (0, \frac{\zeta_z}{4}), \\ C_2 &= (\frac{\zeta_x}{2}, -\frac{\zeta_z}{4}),\end{aligned} \tag{52}$$

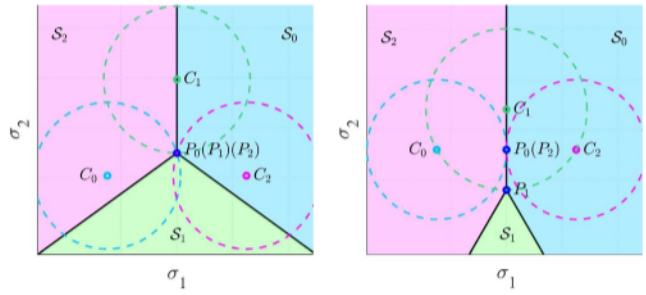

(a) When $\boldsymbol{u}_\zeta$ satisfies (56), h_0, h_1 and h_2 obtain the same minimal value at the same point in the nullspace.

(b) When $\boldsymbol{u}_\zeta$ satisfies (58), h_0 and h_2 obtain the same minimal value at the same point in the nullspace.

Fig. 3. Geometric interpretation of the presented min–max optimization. (For interpretation of the references to color in this figure legend, the reader is referred to the web version of this article.)

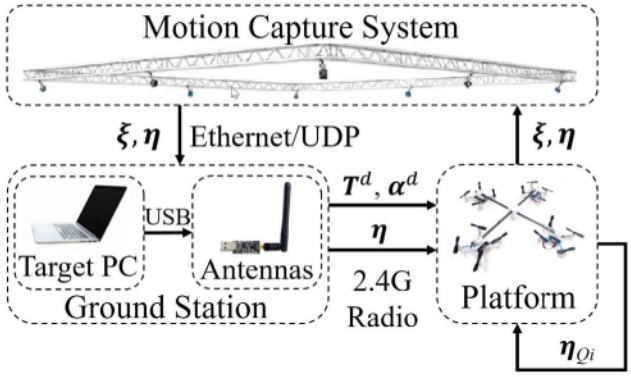

Fig. 4. Experiment setup. The motion capture system measures the position and attitude of the platform central frame, and send the data to the target PC through Ethernet, where the position and attitude controllers in addition to the input allocator run. The inner-loop reference signals are sent to each quadcopter through 2.4G radio. The inner-loop tracking controllers run onboard each quadcopter.

in the (σ_1, σ_2) space, and S_0, S_1 and S_2 are marked in cyan, green and pink respectively. According to (44), h_0 is equivalent to the minimal distance between C_0 and an arbitrary point $P \in S_0$, as

$$h_0 = \min_{P \in S_0} C_0 P = C_0 P_0. \tag{53}$$

Similarly,

$$h_1 = \min_{P \in S_1} C_1 P = C_1 P_1, \tag{54}$$

$$h_2 = \min_{P \in S_2} C_2 P = C_2 P_2. \tag{55}$$

Here P_0, P_1 and P_2 stands for the optimal point in the nullspace (σ_1, σ_2) where the minimal values h_0, h_1 and h_2 are obtained. It can be observed from Fig. 3 that the optimal point varies with a different selection of $\boldsymbol{u}_\zeta$. When

$$-\frac{\zeta_z}{4} \le -\frac{\zeta_x^2}{4\zeta_z}, \tag{56}$$

h_0, h_1 and h_2 obtain the same minimal value at the same point

$$(\sigma_1^{opt}, \sigma_2^{opt}) = P_0 = P_1 = P_2 = (0, -\frac{\zeta_x^2}{4\zeta_z}), \tag{57}$$

as shown in Fig. 3(a).

On the other hand, when

$$-\frac{\zeta_z}{4} > -\frac{\zeta_x^2}{4\zeta_z}, \tag{58}$$

h_0 and h_2 obtain the same minimal value at the same point

$$(\sigma_1^{opt}, \sigma_2^{opt}) = P_0 = P_2 = (0, -\frac{\zeta_z}{4}), \tag{59}$$

as shown in Fig. 3(b).

Therefore, the optimal solution for the min–max optimization (42) is

$$(\sigma_1^{opt}, \sigma_2^{opt}) = \begin{cases} (0, -\zeta_x^2/(4\zeta_z)) & \text{when (56) holds} \\ (0, -\zeta_z/4) & \text{when (58) holds.} \end{cases} \tag{60}$$

The corresponding optimal allocation can be expressed as

$$T_i^d = \sqrt{F_{si}^2 + (F_{ci} + (-1)^{i+1}\sigma_2^{opt})^2}, \tag{61}$$

for the desired thrust forces and

$$\alpha_i^d = \text{atan2}(F_{si}, F_{ci} + (-1)^{i+1}\sigma_2^{opt}), \tag{62}$$

for the desired tilting angles, where F_{si} and F_{ci} refers to the least-square allocation results.

4. Simulations and experiments

To demonstrate the effectiveness of the presented configuration and the control/allocation scheme, simulations and experiments are conducted. This section concludes the results of three tests: (1) The independent tracking of six DoF trajectories to verify the full actuation functionality of the presented configuration; (2) The maximum reachable inclination angle under the proposed allocation in comparison with the regular least-square allocation to verify our control advantages on suppressing the maximum required thrust and thus enlarging the operational space under input saturation; (3) The recovery under external impulse disturbance to verify the stability of the control architecture.

4.1. Setups

Simulations and experiments are conducted on the prototype built in UCLA MacLab [29], where Crazyflie 2.1 [37], of which the key parameters are tested in [38], are selected as the quadcopter module. The prototype critical parameters are listed in Table 2. For experiments, the central controller runs on the Ubuntu 16.04 operating system on the target PC. The control commands are sent to each quadcopter via the Crazy Radio PA antennas through 2.4 G radio. Quadcopter controllers run on the onboard STM32. An Optitrack motion capture system is used for position and attitude measurements in the indoor environment, and communicates with the target PC through Ethernet. The PC-quadcopter communication rate is set to 100 Hz. The outer-loop controller runs at 100 Hz. Quadcopter controllers run at 500 Hz to ensure fast inner-loop response. The system is demonstrated in Fig. 4.

The simulation model includes the gyroscopic effect of the frame, motor inner dynamics and saturation of motor speed, which are neglected in the model for controller design. Offsets of quadcopters' center of mass with respect to the hinge axis are calculated by quadcopters' free responses along passive hinges. A communication delay of 20 ms is added in the simulation model [28]. Representative sensor noises are also included [30].

4.2. Test 1: Independent tracking of six DoF trajectories

The major desired functionality of the presented platform configuration is full actuation, e.g. the capability to track six DoF trajectories independently. Test 1 designs six reference trajectories for the six DoF respectively, each of which contains multiple line segments connected with non-differentiable connecting points to explore the tracking performance in both low and high frequencies. Overlay of snapshots in test 1 are demonstrated in Fig. 6.

Table 2
Critical parameters of the prototype for simulations and experiments.

Parameter	Value
m	0.16 kg
l	0.14 m
a	4.60 cm
I_{xx}	1.46×10^{-3} kg m^2
I_{yy}	1.46×10^{-3} kg m^2
I_{zz}	2.77×10^{-3} kg m^2
T^M	0.55 N

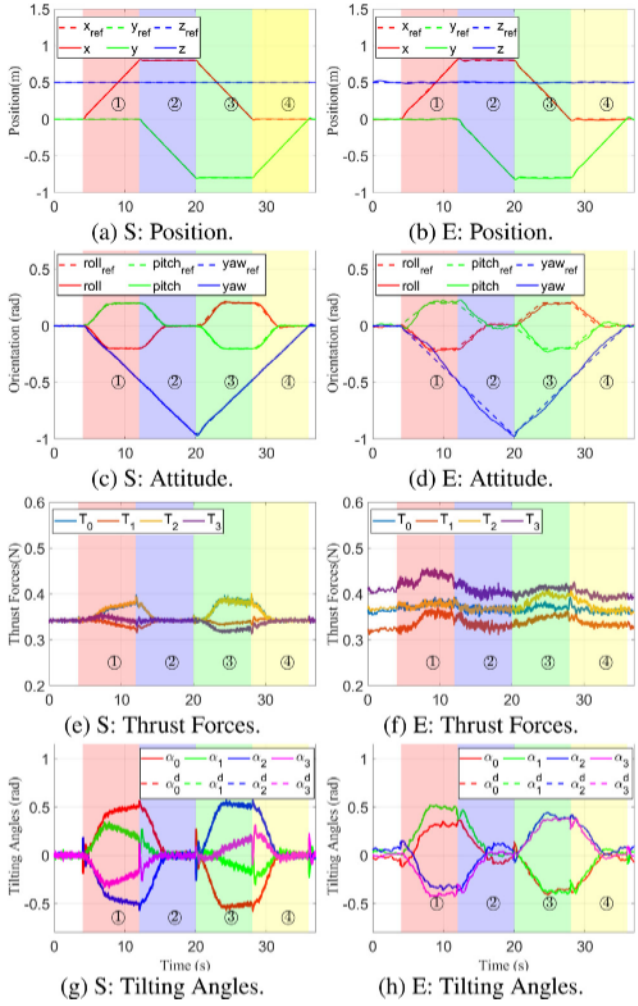

Fig. 5. Test 1 results: tracking six DoF independent trajectories in simulation (S) and experiment (E).

The tracking performances in simulation and experiment are shown in Fig. 5. Consistency of the results indicates the validation of the presented dynamic model and the controller. The Rooted-Mean-Square (RMS) tracking errors are summarized in Table 3. The performance is comparable with the state-of-the-art works [20,21]. Furthermore, compared with the controller previously designed on the same prototype [29], the RMS error under the same trajectory is significantly decreased, especially in the x (95% in S, 83% in E) and the y (94% in S, 83% in E) directions.

4.3. Test 2: Maximum inclination angle

All strict allocation methods from virtual inputs $\boldsymbol{u}_\xi$ and $\boldsymbol{u}_\nu$ by exploring the nullspace (40) are supposed to be equivalent under the ideal case where thrust forces do not have limitations. However, that is not the case in practice. As the thrust efficiency of tilting cant angle multirotor platforms decreases with increasing platform attitude [22], suppressing the maximum required thrust force will result in a larger operational space under the same thrust limit.

This test compares the operational spaces under the proposed min–max allocation and the regular least-square allocation by testing the maximum inclination angle in the pitch direction. During the test, the prototype initiates by hovering at a fixed point with zero attitude. The prototype pitch angle then increases by tracking a ramp trajectory until flight failure occurs, when either position or attitude errors exceed the tolerance boundaries [28]. The largest pitch angle before failure is defined as the maximum inclination angle under one certain allocation method.

Test 2 is conducted in both simulation and experiment, and the results are shown in Fig. 7. It can be observed that (1) the maximum inclination angle of the proposed allocation method shows an increase compared with the least-square allocation in both simulation (0.11 rad or 17%) and experiment (0.14 rad or 33%); (2) the proposed allocation, compared with the least-square allocation, does suppress the maximum required thrust force for the same desired pitch angle; (3) the simulation results match with the experiment results. These observations verify that the proposed allocation method suppresses the maximum required thrust force and results in a larger operational space under thrust limitations in contrast with the least-square allocation.

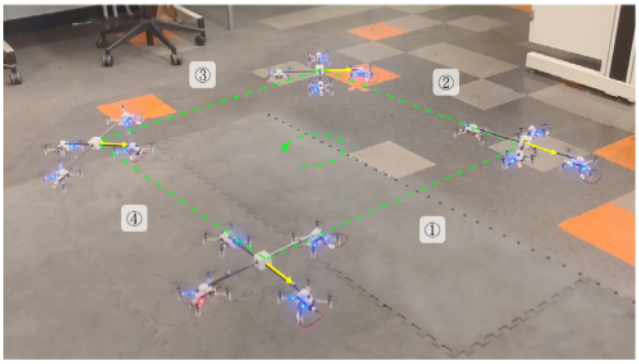

Fig. 6. Overlay of snapshots in the experiment of test 1, where the prototype in each DoF tracks an independent trajectory. ①-④ indicate the corresponding regions in Fig. 5.

Table 3
Six DoF RMS tracking errors of test 1 in simulation (S) and experiment (E).

	x (mm)	y (mm)	z (mm)	Roll (rad)	Pitch (rad)	Yaw (rad)
S	2.60	2.63	1.62	0.008	0.007	0.006
E	9.00	6.90	6.13	0.017	0.026	0.030

4.4. Test 3: Recovery under impulse disturbance

The stability of the presented hierarchical control architecture can be demonstrated by the response of an impulse disturbance, as shown in Fig. 8. The disturbance is created by artificially injecting additive signals to the original inputs in the experiment, as shown in Fig. 8(a). The thrust forces T_1 and T_3 are biased by 0.02 N and -0.05 N from 1s to 1.3s respectively, which is equivalent to injecting an impulse disturbance force and impulse disturbance torque simultaneously to the platform. It can be observed that both position and attitude in all six DoF are deviated and recovered to the initial states, indicating the stability of the controller and its robustness under external disturbances. The impulse response also shows that the low-level dynamics is much faster than the high-level position and attitude controllers.

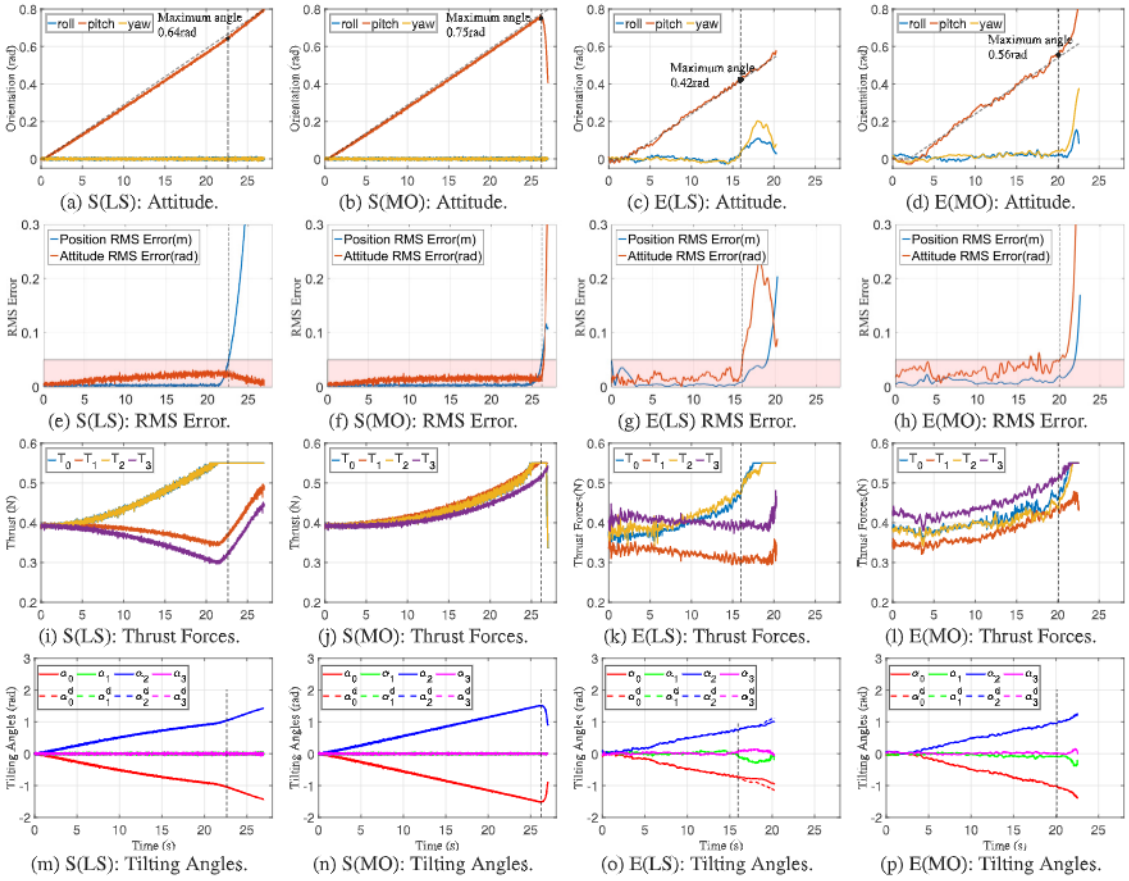

Fig. 7. Test 2 results: reaching the maximum inclination angle under the least-square (LS) allocation and the proposed min–max optimal (MO) allocation, in simulation (S) and experiment (E).

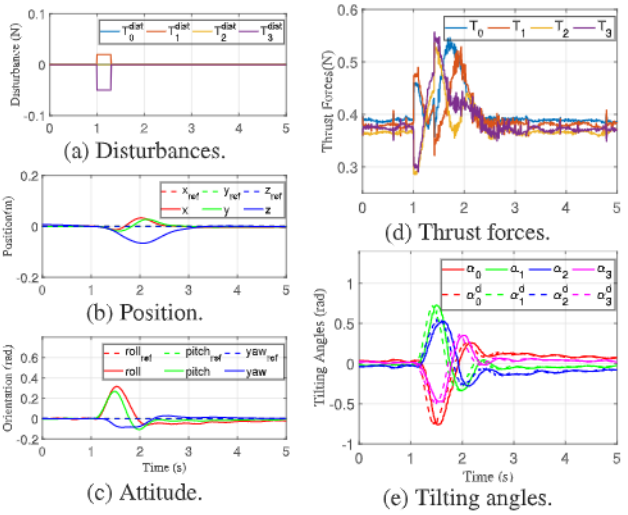

Fig. 8. Test 3 results: Recovery under an impulse disturbance in both position and attitude at hovering in experiment.

5. Discussion

This paper presented a novel configuration of fully actuated multi-rotor aerial platform, which replaces the propeller–rotor pair and tilting motor in the existing configurations [20–22] with regular quadcopter mounted on a passive hinge. The presented configuration largely reduces the difficulties of design and prototyping of tiltable-rotor aerial platforms, and also eliminates the disturbances from propeller drag, gyroscopic effect and tilting reaction, which are all inevitable for the aforementioned tiltable-rotor platforms. One unique functionality of the presented configuration is the fast auxiliary input, which has been proved to be effective on improving the tracking performance of high-bandwidth Refs. [32] and recovering from actuator failure [33].

However, one common limitation of all one DoF tiltable-rotor aerial platforms, including [20,21] and the presented one, is that the thrust efficiency decreases when the attitude becomes larger. Therefore, when the thrust force is limited, the operational space will be constrained. This can be improved by either algorithms or mechanisms. As for the algorithm, this paper proposed an min–max optimal allocation method that fits all one DoF tiltable-rotor aerial platforms. The new allocation method can improve the operational space under thrust saturation compared with the least-square method [21]. As for the mechanism, [27] applied universal joints to connect multiple quadcopters, but the operational space is still constrained by the limited range of the joint. [30] proposed a two DoF passive gimbal joint for universal rotation and achieves higher thrust efficiency, but increased the mechanical complexity and structural compliance, and sacrificed the auxiliary inputs for tracking performance improvement and actuator failure recovery.

The hierarchical control architecture applied in this paper has been widely used for tiltable-rotor aerial platforms [21,22,30,39]. However, the stability and robustness remain challenging issues. Apart from the robustness from the high-level LQRi controllers when the low-level tracking bandwidth is sufficient, a quantitative criterion for robust stability is proposed in this paper to take into account the overall effect of high-level and low-level dynamics, thus can be used to design robust controllers to handle model uncertainty and disturbance rejection. However, it should be noticed that the disturbance rejection capability can be better addressed by explicitly introducing disturbance in the

controller design, as presented in [40], which can be one important direction for the future works.

The tracking performance of the proposed controller reaches the level of the state-of-the-arts [20,21]. However, compared with regular quadcopters, the performance still has room for improvement. This can be one promising future direction of this work, to elevate the accuracy either by more advanced control algorithms [41] or estimation of disturbances and uncertainties [42,43].

6. Conclusion

The presented tilting-thrust actuator module is simple in the mechanical design and the quad-configuration aerial platform in this paper has the full actuation capability for six DoF motions. The dynamics of aerial platforms made up of these modules, when properly configured can be modeled as a single rigid body for the control design. The hierarchical control is effective with the communication latency included in the outer loop control design and the fast inner loop actuator dynamics. A quantitative stability criterion is presented for controller design. Our actuator modules with quadcopters mounted on passive hinges have the advantages that the passive hinges do not transmit to the platform — the hinge rotation torque, the rotor's aerodynamic drag torque, and the rotor's gyroscopic torque when changing orientations. As such the accurate multi-body dynamics of the platform facilitates the model-based control without these terms considered as disturbances or unmodeled dynamics.

The optimal control allocation for the over-actuated aerial platform, in the least-square or min–max formulation, has been experimentally validated to be effective until hitting the thrust saturation constraints. Both closed form solutions are efficient in computation without resorting to numerical iterations. Subject to the thrust saturation limits against the total weight, the maximum inclination angle achieved by the min–max allocation is larger than that achieved by the least-square allocation. Any arbitrary platform attitude angle would have been achievable had the thrust force been sufficiently large to overcome gravity, thanks to the unlimited range of the passive hinge rotations.

The general agreements in the simulation and experimental results suggest that the modeling is adequate for the model-based control design with the unmodeled factors in check.

CRediT authorship contribution statement

Lecheng Ruan: Conceptualization, Methodology, Writing – original draft, Writing – reviewing & editing. **Chen-Huan Pi:** Software, Validation. **Yao Su:** Software, Visualization, Writing – original draft. **Pengkang Yu:** Software, Visualization, Writing – reviewing & editing. **Stone Cheng:** Supervision, Writing – reviewing & editing. **Tsu-Chin Tsao:** Conceptualization, Methodology, Writing – reviewing & editing.

Data availability

Data will be made available on request.

Acknowledgments

The authors would like to appreciate Dr. Wenzhong Yan and Dr. Ankur Mehta for the access and assistance in the motion capture system.

Declaration of competing interest

The authors declare that they have no known competing financial interests or personal relationships that could have appeared to influence the work reported in this paper.

References

[1] Mellinger D, Kumar V. Minimum snap trajectory generation and control for quadrotors. In: Proceedings of international conference on robotics and automation. 2011.

[2] Mahony R, Kumar V, Corke P. Multirotor aerial vehicles: Modeling, estimation, and control of quadrotor. IEEE Robot Autom Mag 2012;19(3):20–32.

[3] Hua M-D, Hamel T, Morin P, Samson C. Introduction to feedback control of underactuated VTOLvehicles: A review of basic control design ideas and principles. IEEE Control Syst Mag 2013;33(1):61–75.

[4] Asheralieva A, Niyato D. Game theory and Lyapunov optimization for cloud-based content delivery networks with device-to-device and UAV-enabled caching. IEEE Trans Veh Technol 2019;68(10):10094–110.

[5] Vong CH, Ryan K, Chung H. Trajectory tracking control of quadcopters under tunnel effects. Mechatronics 2021;78:102628.

[6] Talaeizadeh A, Antunes D, Pishkenari HN, Alasty A. Optimal-time quadcopter descent trajectories avoiding the vortex ring and autorotation states. Mechatronics 2020;68:102362.

[7] Nekoo SR, Acosta JÁ, Heredia G, Ollero A. A benchmark mechatronics platform to assess the inspection around pipes with variable pitch quadrotor for industrial sites. Mechatronics 2021;79:102641.

[8] Kwon W, Park JH, Lee M, Her J, Kim S-H, Seo J-W. Robust autonomous navigation of unmanned aerial vehicles (UAVs) for warehouses' inventory application. IEEE Robot Autom Lett 2019;5(1):243–9.

[9] Sawadsitang S, Niyato D, Tan P-S, Wang P. Joint ground and aerial package delivery services: A stochastic optimization approach. IEEE Trans Intell Transp Syst 2018;20(6):2241–54.

[10] Steich K, Kamel M, Beardsley P, Obrist MK, Siegwart R, Lachat T. Tree cavity inspection using aerial robots. In: Proceedings of international conference on intelligent robots and systems. 2016.

[11] Loianno G, Spurny V, Thomas J, Baca T, Thakur D, Hert D, et al. Localization, grasping, and transportation of magnetic objects by a team of mavs in challenging desert-like environments. IEEE Robot Autom Lett 2018;3(3):1576–83.

[12] Jafarinasab M, Sirouspour S, Dyer E. Model-based motion control of a robotic manipulator with a flying multirotor base. IEEE/ASME Trans Mechatronics 2019;24(5):2328–40.

[13] Petrlík M, Báča T, Heřt D, Vrba M, Krajník T, Saska M. A robust uav system for operations in a constrained environment. IEEE Robot Autom Lett 2020;5(2):2169–76.

[14] Rashad R, Califano F, Stramigioli S. Port-hamiltonian passivity-based control on se (3) of a fully actuated UAV for aerial physical interaction near-hovering. IEEE Robot Autom Lett 2019;4(4):4378–85.

[15] Rashad R, Goerres J, Aarts R, Engelen JB, Stramigioli S. Fully actuated multirotor UAVs: A literature review. IEEE Robot Autom Mag 2020;27(3):97–107.

[16] Jiang G, Voyles RM, Choi JJ. Precision fully-actuated uav for visual and physical inspection of structures for nuclear decommissioning and search and rescue. In: IEEE international symposium on safety, security, and rescue robotics. 2018.

[17] Rajappa S, Ryll M, Bülthoff HH, Franchi A. Modeling, control and design optimization for a fully-actuated hexarotor aerial vehicle with tilted propellers. In: Proceedings of international conference on robotics and automation. 2015.

[18] Ryll M, Muscio G, Pierri F, Cataldi E, Antonelli G, Caccavale F, et al. 6D physical interaction with a fully actuated aerial robot. In: Proceedings of international conference on robotics and automation. 2017.

[19] Park S, Lee J, Ahn J, Kim M, Her J, Yang G-H, et al. Odar: Aerial manipulation platform enabling omnidirectional wrench generation. IEEE/ASME Trans Mechatronics 2018;23(4):1907–18.

[20] Ryll M, Bülthoff HH, Giordano PR. A novel overactuated quadrotor unmanned aerial vehicle: Modeling, control, and experimental validation. IEEE Trans Control Syst Technol 2014;23(2):540–56.

[21] Kamel M, Verling S, Elkhatib O, Sprecher C, Wulkop P, Taylor Z, et al. The voliro omniorientational hexacopter: An agile and maneuverable tiltable-rotor aerial vehicle. IEEE Robot Autom Mag 2018;25(4):34–44.

[22] Gerber MJ, Tsao T-C. Twisting and tilting rotors for high-efficiency, thrust-vectored quadrotors. J Mech Robot 2018;10(6):061013.

[23] Ryll M, Bicego D, Franchi A. Modeling and control of FAST-Hex: A fully-actuated by synchronized-tilting hexarotor. In: Proceedings of international conference on intelligent robots and systems. 2016.

[24] Ding C, Lu L. A tilting-rotor unmanned aerial vehicle for enhanced aerial locomotion and manipulation capabilities: Design, control, and applications. IEEE/ASME Trans Mech 2021;26(4):2237–48.

[25] Villa DK, Brandao AS, Sarcinelli-Filho M. A survey on load transportation using multirotor UAVs. J Intell Robot Syst 2019;1–30.

[26] Mohammadi K, Sirouspour S, Grivani A. Control of multiple quad-copters with a cable-suspended payload subject to disturbances. IEEE/ASME Trans Mechatronics 2020;25(4):1709–18.

[27] Nguyen H-N, Park S, Park J, Lee D. A novel robotic platform for aerial manipulation using quadrotors as rotating thrust generators. IEEE Trans Robot 2018;34(2):353–69.
[28] Ruan L. Independent position and attitude control on multirotor aerial platforms (Ph.D. thesis), Los Angeles: University of California; 2020.
[29] Pi C, Ruan L, Yu P, Su Y, Cheng S, Tsao T. A simple six degree-of-freedom aerial vehicle built on quadcopters. In: Proceedings of IEEE conference on control technology applications. 2021.
[30] Yu P, Su Y, Gerber MJ, Ruan L, Tsao T-C. An over-actuated multi-rotor aerial vehicle with unconstrained attitude angles and high thrust efficiencies. IEEE Robot Autom Lett 2021;6(4):6828–35.
[31] Su Y, Yu P, Gerber M, Ruan L, Tsao T-C. Nullspace-based control allocation of overactuated UAV platforms. IEEE Robot Autom Lett 2021;6(4):8094–101.
[32] Su Y, Ruan L, Yu P, Pi C-H, Gerber M, Tsao T-C. A fast and efficient attitude control algorithm of a tilt-rotor aerial platform using inputs redundancies. IEEE Robot Autom Lett 2021.
[33] Su Y. Compensation and control allocation with input saturation limits and rotor faults for multi-rotor copters with redundant actuations [Ph.D. thesis], Los Angeles: University of California; 2021.
[34] Su Y, Yu P, Gerber M, Ruan L, Tsao T. Fault-tolerant control of overactuated multirotor UAV platform under propeller failure. IEEE/ASME Trans Mechatronics 2022. [submitted for publication].
[35] Lee T, Leok M, McClamroch NH. Geometric tracking control of a quadrotor UAV on SE (3). In: Conference on decision and control. 2010.
[36] Albus JS, Barbera AJ, Nagel RN, et al. Theory and practice of hierarchical control. National Bureau of Standards; 1980.
[37] Giernacki W, Skwierczyński M, Witwicki W, Wroński P, Kozierski P. Crazyflie 2.0 quadrotor as a platform for research and education in robotics and control engineering. In: International conference on methods and models in automation and robotics. 2017.
[38] Förster J. System identification of the crazyflie 2.0 nano quadrocopter [B.S. thesis], ETH Zurich; 2015.
[39] Yu P. An over-actuated multi-rotor aerial platform and iterative learning control applications [Ph.D. thesis], Los Angeles: University of California; 2022.
[40] Flores G, de Oca AM, Flores A. Robust nonlinear control for the fully actuated hexa-rotor: Theory and experiments. IEEE Control Syst Lett 2022;7:277–82.
[41] Tal E, Karaman S. Accurate tracking of aggressive quadrotor trajectories using incremental nonlinear dynamic inversion and differential flatness. IEEE Trans Control Syst Technol 2020;29(3):1203–18.
[42] Torrente G, Kaufmann E, Föhn P, Scaramuzza D. Data-driven mpc for quadrotors. IEEE Robot Autom Lett 2021;6(2):3769–76.
[43] Su Y, Chu C, Wang M, Liu Y, Zhu Y, Liu H. Downwash-aware control allocation for over-actuated uav platforms. In: Proceedings of international conference on intelligent robots and systems. 2022.

Lecheng Ruan received the B.S. honor degree from the School of Mechatronic Engineering, Harbin Institute of Technology in 2015, and the Ph.D. degree from the Department of Mechanical and Aerospace Engineering, University of California, Los Angeles in 2020. He is now affiliated with Beijing Institute for General Artificial Intelligence and Peking University. His research interests include control and optimization, mechatronics, robotics, perception and signal processing.

Chen-Huan Pi received the B.S. degree in mechanical engineering and the Ph.D. degree in control science and engineering at the Institute of Mechanical Engineering from National Chiao Tung University, HsinChu in 2015 and 2021 respectively. He worked as a visiting researcher in Aerospace Engineering Department, University of California, Los Angeles in 2019–2020. His research interests include intelligent control of multi-rotor unmanned aerial vehicles.

Yao Su received the B.S. degree from the School of Mechatronic Engineering, Harbin Institute of Technology in 2016, and the M.S. and Ph.D. degrees from the Department of Mechanical and Aerospace Engineering, University of California, Los Angeles in 2017 and 2021. He is now a research scientist at Beijing Institute for General Artificial Intelligence. His research interests include robotics, control, planning, and optimization.

Pengkang Yu received the B.Eng. degree in Mechanical Engineering from Hong Kong University of Science and Technology, Hong Kong, in 2016. He received the M.S. degree and the Ph.D. degree in Mechanical Engineering from the University of California, Los Angeles in 2017 and 2022 respectively. His research interests include control, optimization, planning, robotics and mechatronics.

Stone Cheng received the B.Sc and M.Sc. degrees in Control Engineering from the National Chiao Tung University, HsinChu, in 1981 and 1983, respectively, and the Ph.D. degree in electrical engineering from Manchester University, UK in 1994. He is currently a Professor with the Department of Mechanical Engineering, National Yang Ming Chiao Tung University. His current research interests include motion control, reinforcement learning, and the wide-band-gap semiconductor power device.

Tsu-Chin Tsao received the B.S. degree in engineering from National Taiwan University, Taipei, in 1981, and the M.S. and Ph.D. degrees in mechanical engineering from the University of California, Berkeley, in 1984 and 1988, respectively. He is currently a Professor with the Mechanical and Aerospace Engineering Department, University of California, Los Angeles. His research interests include precision motion control, mechatronics, and robotics. Professor Tsao is a Fellow of ASME and a Senior Member of IEEE.